Low Dose CT Image Denoising Using a Generative Adversarial Network with Wasserstein Distance and Perceptual Loss

Qingsong Yang, Pingkun Yan*, Yanbo Zhang, Hengyong Yu, Yongyi Shi, Xuanqin Mou, Mannudeep K. Kalra, and Ge Wang

Abstract—The continuous development and extensive use of CT in medical practice has raised a public concern over the associated radiation dose to the patient. Reduction of the radiation dose may lead to increased noise and artifacts, which can adversely affect the radiologists judgement and confidence. Hence, advanced image reconstruction from low-dose CT data is needed to improve the diagnostic performance, which is a challenging problem due to its ill-posed nature. Over the past years, various low-dose CT methods have produced impressive results. However, most of the algorithms developed for this application, including the recently popularized deep learning techniques, aim for minimizing the mean-squared-error (MSE) between a denoised CT image and the ground truth under generic penalties. Although the peak signal-to-noise ratio (PSNR) is improved, MSE- or weighted-MSE-based methods can compromise the visibility of important structural details after aggressive denoising. In this paper, we introduce a new CT image denoising method based on the generative adversarial network (GAN) with Wasserstein distance and perceptual similarity. The Wasserstein distance is a key concept of the optimal transform theory, and promises to improve the performance of the GAN. The perceptual loss compares the perceptual features of a denoised output against those of the ground truth in an established feature space, while the GAN helps migrate the data noise distribution from strong to weak. Therefore, our proposed method transfers our knowledge of visual perception to the image denoising task, is capable of not only reducing the image noise level but also keeping the critical information at the same time. Promising results have been obtained in our experiments with clinical CT images.

Index Terms—Low dose CT, Image denoising, Deep learning, Perceptual loss, WGAN

I. INTRODUCTION

RAY computed tomography (CT) is one of the most important imaging modalities in modern hospitals and clinics. However, there is a potential radiation risk to the patient, since x-rays could cause genetic damage and induce

- Q. Yang and G. Wang are with Department of Biomedical Engineering, Rensselaer Polytechnic Institute, Troy, NY, 12180 (e-mail: yangq4@rpi.edu, wangg6@rpi.edu)
- P. Yan* is with Philips Research North America, Bethesda, MD, USA, (email: pingkun@gmail.com)
- Y. Zhang and H. Yu are with the Department of Electrical and Computer Engineering, University of Massachusetts Lowell, Lowell, MA 01854 (email:yanbo_zhang@uml.edu, hengyong-yu@ieee.org)
- Y. Shi and X. Mou are with the Institute of Image Processing and Pattern Recognition, Xian Jiaotong University, Xian, Shaanxi 710049, China (email: xqmou@mail.xjtu.edu.cn)
- M. K. Kalra is with Department of Radiology, Massachusetts General Hospital, Harvard Medical School, Boston, MA, USA(email: mkalra@mgh.harvard.edu)

cancer in a probability related to the radiation dose [1], [2]. Lowering the radiation dose increases the noise and artifacts in reconstructed images, which can compromise diagnostic information. Hence, extensive efforts have been made to design better image reconstruction or image processing methods for low-dose CT (LDCT). These methods generally fall into three categories: (a) sinogram filtration before reconstruction [3]–[5], (b) iterative reconstruction [6], [7], and (c) image post-processing after reconstruction [8]–[10].

Over the past decade, researchers were dedicated to developing new iterative algorithms (IR) for LDCT image reconstruction. Generally, those algorithms optimize an objective function that incorporates an accurate system model [11], [12], a statistical noise model [13]–[15] and prior information in the image domain. Popular image priors include variation (TV) and its variants [16]–[18], as well as dictionary learning [19], [20]. These iterative reconstruction algorithms greatly improved image quality but they may still lose some details and suffer from remaining artifacts. Also, they perform at a high computational cost, which is a bottleneck in practical applications.

On the other hand, sinogram pre-filtration and image postprocessing are computationally efficient compared to iterative reconstruction. Noise characteristic was well modeled in the sinogram domain for sinogram-domain filtration. However, sinogram data of commercial scanners are not readily available, and these methods may suffer from resolution loss and edge blurring. Any operation in the sinogram domain must be carefully taken, because the reconstruction process is very sensitive to even a single incorrect projection value.

Differently from sinogram denoising, image post-processing directly operates on an image, and is not pixel-sensitive. Many efforts were made in the image domain to reduce LDCT noise and suppress artifacts. For example, the non-local means (NLM) method was adapted for CT image denoising [8]. Based on the compressed sensing theory, an adapted K-SVD method was proposed [9] to reduce artifacts in CT images. The block-matching 3D (BM3D) algorithm was used for image restoration in several CT imaging tasks [10]. With such image post-processing, image quality improvement was clear but over-smoothing and/or residual errors were often observed in the processed images. These issues are difficult to address, given the non-uniform distribution of CT image noise.

The recent explosive development of deep neural networks suggests new thinking and huge potential for the medical imaging field [21], [22]. As an example, the LDCT denoising problem can be solved using deep learning techniques. Specifically, the convolutional neural network (CNN) for image super-resolution [23] was recently adapted for low-dose CT image denoising [24], with a significant performance gain. Then, more complex networks were proposed to handle the LDCT denoising problem such as the U-shape network in [25], [26] and the wavelet network in [27].

Despite the impressive denoising results with these innovative network structures, they fall into a category of an end-to-end network that typically uses the mean squared error (MSE) between the network output and the ground truth as the loss function. As revealed by the recent work [28], [29], this per-pixel MSE is often associated with over-smoothed edges and loss of details. As an algorithm tries to minimize per-pixel MSE, it overlooks subtle image textures/signatures critical for human perception. In fact, the CT images are usually distributed over some manifolds, while the MSE approach tends to take the mean of high-resolution patches in the Euclidean space. Therefore, in addition to the blurring effect, artifacts are also possible such as non-uniform biases.

In order to tackle the above problems, here we propose to use a generative adversarial network (WGAN) [30] with the Wasserstein distance as the discrepancy measure between distributions and a perceptual loss that computes the difference between images in an established feature space [28], [29].

The use of WGAN is to ensure that denoised CT images share the same distribution as that of normal dose CT (NDCT) images. In a GAN framework, a generative network G and a discriminator network D are coupled tightly and trained simultaneously. While the G network is trained to produce realistic images G(z) from a random vector z, the D network is trained to discriminate between real and generated images [31], [32]. Up to now, GANs have been used in many applications such as single image super-resolution [28], art creation [33], [34], and image transformation [35]. In the field of medical imaging, Nie $et\ al.$ proposed to use GAN to estimate CT image from its corresponding MR image [36].

Despite its success in these areas, GANs still suffer from a remarkable difficulty in training [32], [37]. In the original GAN [31], D and G are trained by solving the following minimax problem

$$\min_{G} \max_{D} L(D, G) = \mathbb{E}_{\boldsymbol{x} \sim P_r}[\log D(\boldsymbol{x})] + \mathbb{E}_{\boldsymbol{z} \sim P_a}[\log (1 - D(\boldsymbol{z}))] \quad (1)$$

where P_r and P_g are the real data distribution and the generated counterpart. When D is trained to become an optimal discriminator for a fixed G, the minimization search for G is equivalent to minimize the Jensen-Shannon divergence (JSD) of P_r and P_g , which will lead to vanished gradient on the generator G [37] .

An alternative method to train G is by minimizing

$$\mathbb{E}[-\log D(G(z))] \tag{2}$$

which is equivalent to minimize $KL(P_g||P_r) - 2JSD(P_r||P_g)$ when D is the optimum. Here, $KL(\cdot)$ stands for the Kullback-Leibler divergence. This cost function is contradictory because

it minimizes the KL divergence but maximizes the JS divergence. Thus, the gradient updates of the generator become unstable [37].

Consequently, Martin *et al.* proposed to use the *Earth-Mover* (EM) distance or Wasserstein metric between the generated image samples and real data for GAN [30], which is referred to as WGAN, because the EM distance is continuous and differentiable almost everywhere under some mild assumptions while neither KL nor JS divergence is. After that, an improved WGAN with *gradient penalty* was proposed [38] to accelerate the convergence.

The rationale behind the perceptual loss is two-fold. First, when a person compares two images, the perception is not performed pixel-by-pixel. Human vision actually extracts and compares features from images [39]. Therefore, instead of using pixel-wise MSE, we employ another pre-trained deep CNN (the famous VGG [40]) for feature extraction and compare the denoised output against the ground truth in terms of the extracted features. Second, from a mathematical point of view, CT images are not uniformly distributed in a highdimensional Euclidean space. They reside more likely in a low-dimensional manifold. With MSE, we are not measuring the intrinsic similarity between the images, but just their superficial differences in the brute-force Euclidean distance. By comparing images according their intrinsic structures, we should project them onto a manifold and calculate the geodesic distance instead. Therefore, the use of the perceptual loss for WGAN should facilitate producing results with not only lower noise but also sharper details.

In particular, we treat the LDCT denoising problem as a transformation from LDCT to NDCT images. WGAN provides a good distance estimation between the LDCT and NDCT image distributions. Meanwhile, the VGG-based perceptual loss can guarantee that the information content of an image is kept after denoising. The rest of this paper is organized as follows. The proposed method is described in Section II. The experiments and results are presented in Section III. Finally, relevant issues are discussed and a conclusion is drawn in Section IV.

II. METHODS

A. Noise Reduction Model

Let $z \in \mathbb{R}^{N \times N}$ denote a LDCT image and $x \in \mathbb{R}^{N \times N}$ denote the corresponding NDCT image. The goal of the denoising process is to seek a function G that maps LDCT z to NDCT x:

$$G: \mathbf{z} \to \mathbf{x}$$
 (3)

On the other hand, we can also take z as a sample from the LDCT image distribution P_L and x from the NDCT distribution or the real distribution P_r . The denoising function G maps samples from P_L into a certain distribution P_g . By varying the function G, we change P_g to make it close to P_r . In this way, we treat the denoising operator as moving one data distribution to another.

Typically, noise in x-ray photon measurements can be simply modeled as the combination of Poisson quantum noise and Gaussian electronic noise. On the contrary, in the reconstructed

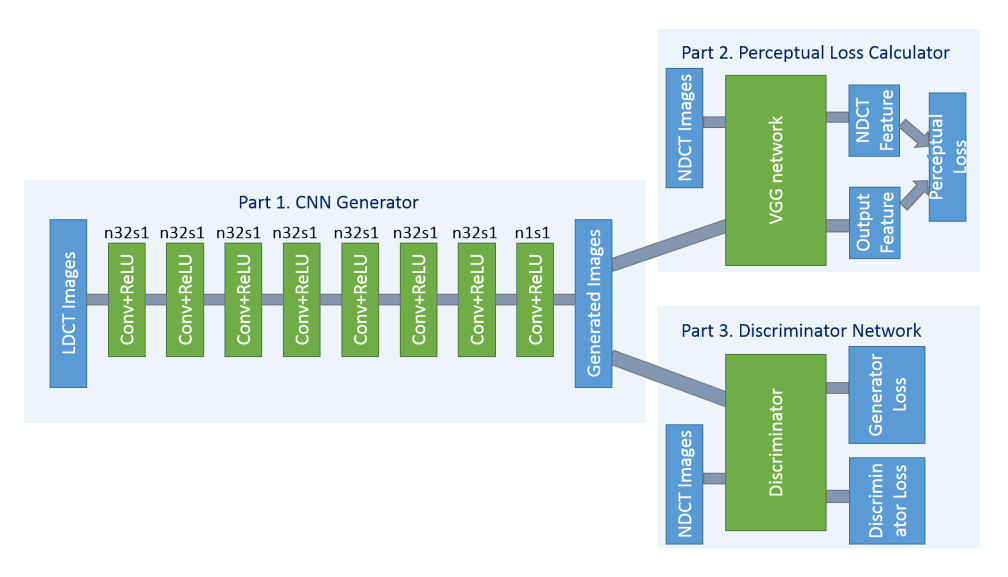


Fig. 1. The overall structure of the proposed WGAN-VGG network.

images, the noise model is usually complicated and non-uniformly distributed across the whole image. Thus there is no clear clue that indicates how data distributions of NDCT and LDCT images are related to each other, which makes it difficult to denoise LDCT images using traditional methods. However, this uncertainty of noise model can be ignored in deep learning denoising because a deep neural network itself can efficiently learn high-level features and a representation of data distribution from pixel data through a hierarchical network.

B. WGAN

Compared to the original GAN network, WGAN uses the Wasserstein distance instead of the JS divergence to compare data distributions. Despite its complicated mathematical derivation [30], the actual implementation of the Wasserstein distance in the GAN needs only three changes:

- Remove the last sigmoid layer in the discriminator D;
- Remove the log in the loss functions of the discriminator D;
- The weights of the D network are clipped to be within [-c,c] after each update of the discriminator, where c is a constant;

The first two changes are consistent with the Wasserstein distance, and the third change is a practical method to optimize the Wasserstein distance. Later on, the weight clipping method was refined by a constraint on the gradient of the discriminator D in the loss function to increase the convergence speed of WGAN,

$$L_{WGAN}(D) = -\mathbb{E}[D(\boldsymbol{x})] + \mathbb{E}[D(G(\boldsymbol{z}))] + \lambda \mathbb{E}[(||\nabla_{\hat{\boldsymbol{x}}}D(\hat{\boldsymbol{x}})||_2 - 1)^2] \quad (4)$$

where the last term is the gradient penalty term and \hat{x} is uniformly sampled along straight lines pairs of generated and real samples. And λ is a constant parameter.

The loss function for the generator disregards the log function in Eq. (2) and is the expressed as

$$L_{WGAN}(G) = -\mathbb{E}[D(G(z))] \tag{5}$$

C. Perceptual Loss

While the WGAN network insures that the generator transforms the data distribution from high noise to a low noise version, another loss function needs to be added for the network to keep image details or information content. Typically, a mean squared error (MSE) loss function is used, which tries to minimize pixel-wise errors between generated and ground truth images [24], [41],

$$L_{MSE} = \frac{1}{N^2} ||G(\boldsymbol{z}) - \boldsymbol{x}||_F^2.$$
 (6)

However, the MSE loss can potentially generate blurry images and cause the distortion or loss of details. Thus, instead of using a MSE measure, we apply a perceptual loss function defined in a feature space,

$$L_{Perceptual} = \frac{1}{whd} ||\phi(G(z)) - \phi(x)||_F^2$$
 (7)

where, ϕ is a feature extractor, and w, h, and d stands for the width, height and depth of the feature space, respectively. In our implementation, we adopt the well-known pre-trained VGG-19 network [40] as the feature extractor. VGG-19 network contains 16 convolutional layers followed by 3 fully-connected layers. We use the 16th convolutional layers as our feature extractor. Thus, the perceptual loss function we used is

$$L_{VGG} = \frac{1}{whd} ||VGG(G(\boldsymbol{z})) - VGG(\boldsymbol{x})||_F^2$$
 (8)

For convenience, we call the perceptual loss computed by VGG network VGG loss.

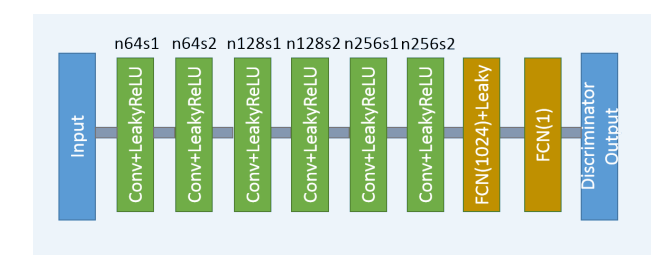


Fig. 2. The structure of the discriminator network.

D. Network Structures

The overall view of the proposed network structure is shown in Fig. 1. For convenience, we name this network WGAN-VGG. It consists three parts. The first part is the generator G, which is a convolutional neural network (CNN) of 8 convolutional layers. Following the common practice in the deep learning community [42], small 3×3 kernels were used in each convolutional layer. Due to the stacking structure, such a network can cover a large enough receptive field efficiently. Each of the first 7 hidden layers of G have 32 filters. The last layer generates only one feature map with a single 3×3 filter, which is also the output of G. We use Rectified Linear Unit (ReLU) as the activation function.

The second part of the network is the perceptual loss calculator, which is realized by the pre-trained VGG network [40]. A denoised output image G(z) from the generator Gand the ground truth image x are fed into the pre-trained VGG network for feature extraction. Then, the objective loss is computed using the extracted features from a specified layer according to Eq. (8). The reconstruction error is then backpropagated to update the weights of G only, while keeping the VGG parameters intact.

The third part of the network is the discriminator D. As shown in Fig. 2, D has 6 convolutional layers. The first two convolutional layers have 64 filters, then followed by two convolutional layers of 128 filters, and the last two convolutional layers have 256 filters. Following the same logic as in G, all the convolutional layers in D have a small 3×3 kernel size. After the six convolutional layers, there are two fully-connected layers, of which the first has 1024 outputs and the other has a single output. Following the practice in [30], there is no sigmoid cross entropy layer at the end of D.

E. Loss Functions

The proposed WGAN-VGG networks involves three subnetworks. While the VGG network is kept the same during the training, the generator G and discriminator D are updated. The loss function of G is

$$L_{WGAN-VGG}(G) = L_{WGAN}(G) + \lambda_1 L_{VGG}(G)$$
 (9)

where λ_1 is a parameter to control the trade-off between the WGAN adversarial loss and the VGG perceptual loss. And the loss function D is same as in Eq. (4)

For comparison purpose, we also trained four other networks.

Require: Set hyperparameters, $\lambda = 10, \alpha = 1 \times 10^{-5}, \beta_1 =$ $0.5, \beta_2 = 0.9, \lambda_1 = 0.1, \lambda_2 = 0.1,$

Require: Set the number of total epochs, $N_{epoch} = 100$, the number of iteration for discriminator training, $N_D = 4$, and the number of batch size, m = 128,

Require: Initial discriminator parameters w_0 , initial generator parameters θ_0

Require: Load VGG-19 network parameters

```
1: for num\_epoch = 0, ..., N_{epoch} do
            for t = 1, ..., N_D do
 2:
                 Sample a batch of NDCT image patches \{x^{(i)}\}_{i=1}^m,
 3:
                 latent LDCT patches \{z^{(i)}\}_{i=1}^m, and random numbers
                 \{\epsilon^{(i)}\}_{i=1}^m \sim Uniform[0,1]
                 for i = 1, ..., m do
 4:
                       \begin{aligned} \hat{\boldsymbol{x}}^{(i)} &\leftarrow \epsilon^{(i)} \boldsymbol{x}^{(i)} + (1 - \epsilon^{(i)}) G(\boldsymbol{z}^{(i)}) \\ L_D^{(i)} &\leftarrow D(G(\boldsymbol{z}^{(i)})) - D(\boldsymbol{x}^{(i)}) + \lambda(||\nabla D(\hat{\boldsymbol{x}}^{(i)})||_2 - \\ 1)^2 \end{aligned} 
 5:
 6:
                 end for
 7:
            end for
 8:
            Update D: w \leftarrow \operatorname{Adam}(\nabla_w \frac{1}{m} \sum_{i=1}^m L_G^{(i)}, w, \alpha, \beta_1, \beta_2)
Sample a batch of LDCT patches \{\boldsymbol{z}^{(i)}\}_{i=1}^m and corre-
 9:
10:
            sponding NDCT patches \{x^{(i)}\}_{i=1}^m,
11:
```

11: **for**
$$i = 1, ..., m$$
 do
12: $L_G^{(i)} \leftarrow \lambda_1 L_{VGG}(\boldsymbol{z}^{(i)}, \boldsymbol{x}^{(i)}) - D(G(\boldsymbol{z}^{(i)}))$
13: **end for**
14: Update $G, \theta \leftarrow \operatorname{Adam}(\nabla_{\theta} \frac{1}{n} \sum_{i=1}^{m} L_G^{(i)}, w, \alpha, \beta_1, \beta_2$

14: Update
$$G$$
, $\theta \leftarrow \operatorname{Adam}(\nabla_{\theta} \frac{1}{m} \sum_{i=1}^{m} L_{G}^{(i)}, w, \alpha, \beta_{1}, \beta_{2})$
15: **end for**

Fig. 3. Optimization procedure of WGAN-VGG network.

CNN-MSE with only MSE loss

$$L_{CNN-MSE}(G) = L_{MSE} \tag{10}$$

CNN-VGG with only VGG loss

$$L_{CNN-VGG}(G) = L_{VGG}(G) \tag{11}$$

WGAN-MSE with MSE loss in the WGAN framework

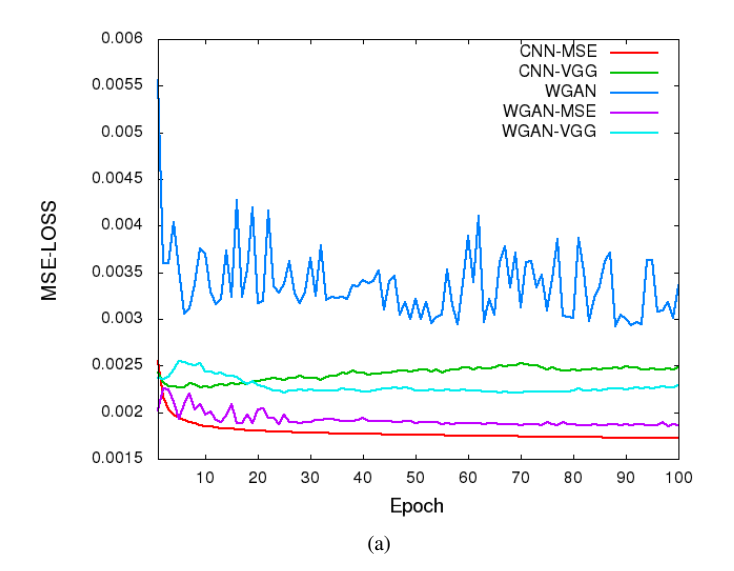
$$L_{WGAN-MSE}(G) = L_{WGAN}(G) + \lambda_2 L_{MSE}(G)$$
 (12)

WGAN without any additive loss function

III. EXPERIMENT

A. Experimental Datasets

We used a real clinical dataset authorized for "the 2016 NIH-AAPM-Mayo Clinic Low Dose CT Grand Challenge" by Mayo Clinic for the training and evaluation of the proposed networks [43]. The dataset contains 10 anonymous patients' normal-dose abdominal CT images and simulated quarterdose CT images. In our experiments, we randomly extracted 100,096 pairs of image patches from 4,000 CT images as our training inputs and labels. The patch size is 64×64 . Also, we extracted 5,056 pairs of patches from another 2,000 patient images for validation. For comparison, we implemented a stateof-the-art 3D dictionary learning reconstruction technique as a representative IR algorithm [19], [20]. The dictionary learning reconstruction was performed from the LDCT projection data provided by Mayo Clinic.



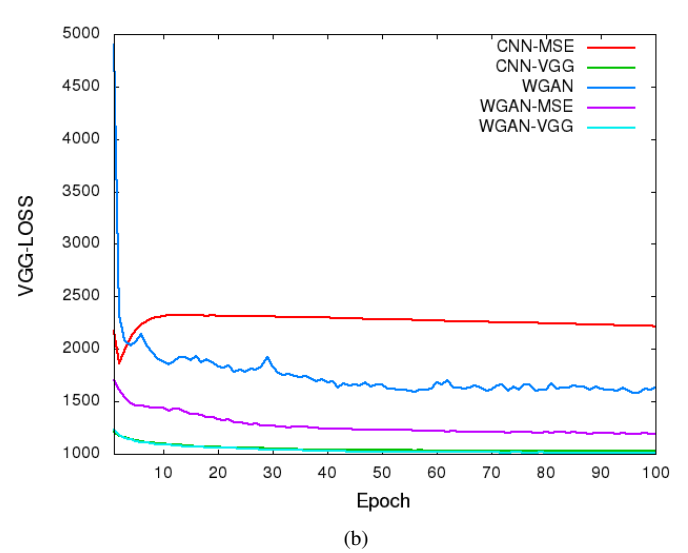


Fig. 4. Plots of validation loss versus the number of epochs during the training of the 5 networks. (a)MSE loss convergence and (b)VGG loss convergence.

B. Network Training

In our experiments, all the networks were optimized using Adam algorithm [44]. The optimization procedure for WGAN-VGG network is shown in Fig. 3. The mini-batch size was 128. The hyperparameters for Adam were set as $\alpha=1e-5, \beta_1=0.5, \beta_2=0.9$, and we chose $\lambda=10$ in Eq. (4) as suggested in [38], $\lambda_1=0.1, \lambda_2=0.1$ in Eqs. (9) and (12) according to our experimental experience. The optimization processes for WGAN-MSE and WGAN are similar except that line 12 was changed to the corresponding loss function, and for CNN-MSE and CNN-VGG, lines 2-10 were removed.

The networks were implemented in Python with the Tensorflow library [45]. A NVIDIA Titan XP GPU was used in this study.

C. Network Convergence

To visualize the convergence of the networks, we calculated the MSE loss and VGG loss over the 5,056 image patches for validation according to Eqs. (6) and (8) after each epoch.

TABLE I
QUANTITATIVE RESULTS ASSOCIATED WITH DIFFERENT NETWORK
OUTPUTS FOR FIGS. 5 AND 7

	Fig. 5			Fig	. 7
	PSNR	SSIM		PSNR	SSIM
LDCT	19.7904	0.7496	-	18.4519	0.6471
CNN-MSE	24.4894	0.7966		23.2649	0.7022
WGAN-MSE	24.0637	0.8090		22.7255	0.7122
CNN-VGG	23.2322	0.7926		22.0950	0.6972
WGAN-VGG	23.3942	0.7923		22.1620	0.6949
WGAN	22.0168	0.7745		20.9051	0.6759
DictRecon	24.2516	0.8148		24.0992	0.7631

TABLE II STATISTICAL PROPERTIES OF THE BLUE RECTANGLE AREAS IN FIGS. 5 $$\operatorname{AND}\ 7$$

	Fig. 5			Fig. 7	
	Mean	SD		Mean	SD
NDCT	9	36	•	118	38
LDCT	11	74		118	66
CNN-MSE	12	18		120	15
WGAN-MSE	9	28		115	25
CNN-VGG	4	30		104	28
WGAN-VGG	9	31		111	29
WGAN	23	37		135	33
DictRecon	4	11		111	13

In Fig. 4, we plotted the averaged MSE and VGG losses respectively versus the number of epochs for the five networks. It should be noted that even though these two loss functions were not used at the same time for a given network, we still want to see how their values change during the training. In the two figures, both the MSE and VGG losses decreased initially, which indicates that the two metrics are positively correlated. However, the loss values of the networks in terms of MSE are increasing in the following order, CNN-MSE<WGAN-MSE<WGAN-VGG<CNN-VGG (Fig. 4a), yet the VGG loss are in the opposite order (Fig. 4b). Moreover, WGAN-VGG and CNN-VGG has very close VGG loss values, while their MSE losses are quite different. On the other hand, WGAN perturbed the convergence as measured by MSE but smoothly converged in terms of VGG loss. These observations suggest that the two metrics have different focuses when being used by the networks. The difference between MSE and VGG losses will be further revealed in the output images of the generators.

D. Denoising Results

To show the denoising effect of the selected networks, we took two representative slices as shown in Figs. 5 and 7. And Figs. 6 and 8 are the zoomed regions-of-interest (ROIs) marked by the red rectangles in Figs. 5 and 7. All the networks demonstrated certain denoising capabilities. However, CNN-MSE blurred the images and introduced waxy artifacts as expected, which are easily observed in the zoomed ROIs in Figs. 6c and 8c. WGAN-MSE was able to improve the result of CNN-MSE by avoiding over-smooth but minor streak artifacts can still be observed especially compared to CNN-VGG and WGAN-VGG. Meanwhile, WGAN generated stronger noise

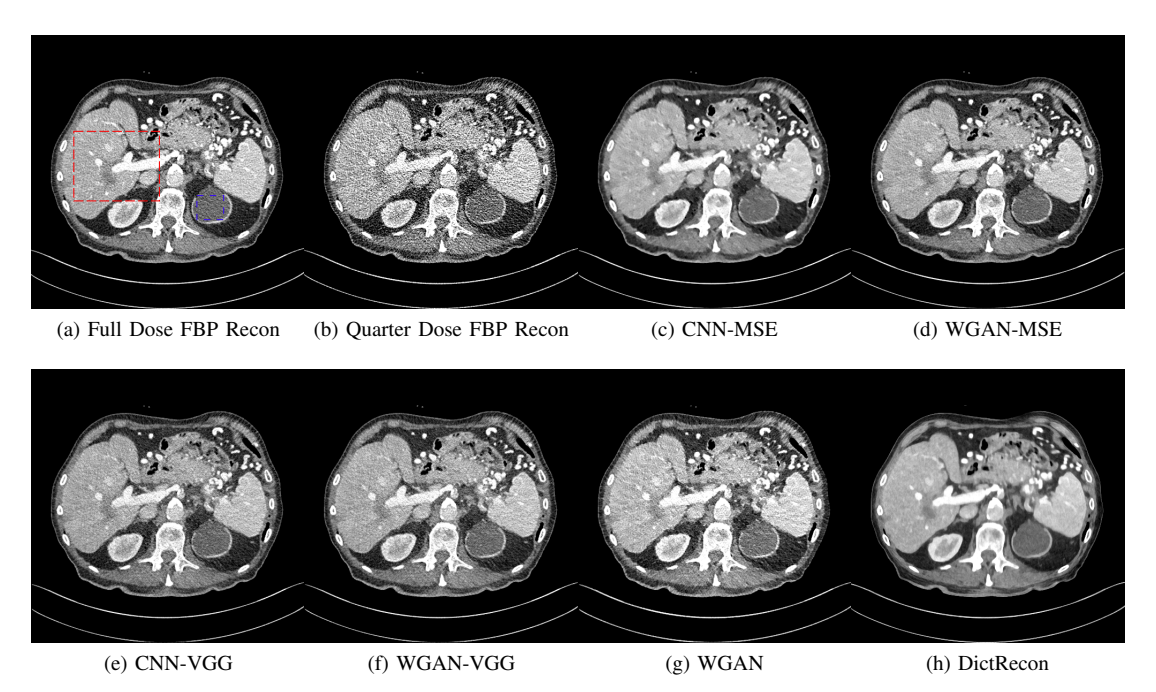


Fig. 5. Transverse CT images of the abdomen demonstrate a low attenuation liver lesion (in the red box) and a cystic lesion in the upper pole of the left kidney (in the blue box). This display window is [-160, 240]HU.

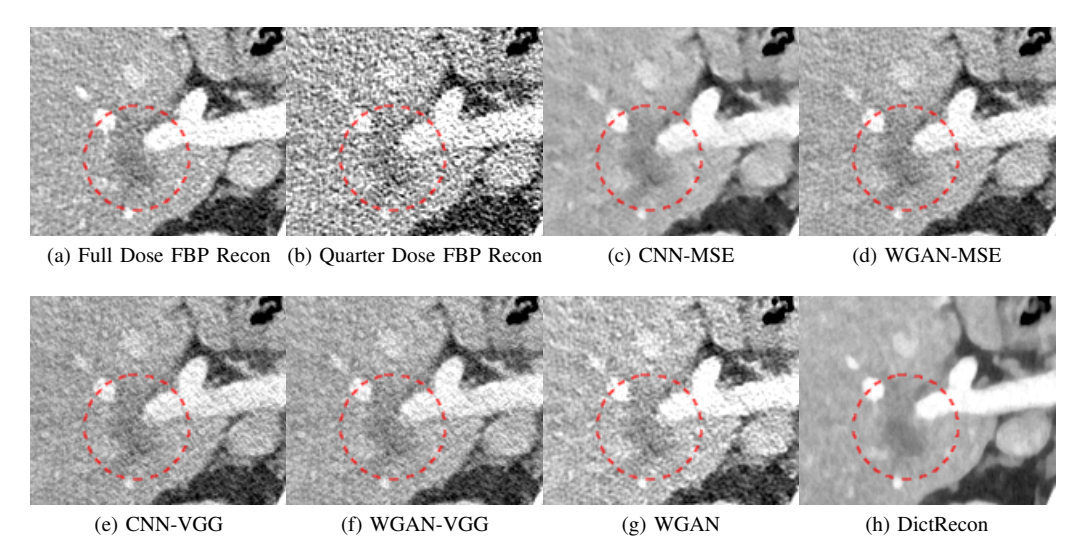


Fig. 6. Zoomed ROI of the red rectangle in Fig. 5. The low attenuation liver lesion with in the dashed circle represents metastasis. The lesion is difficult to assess on quarter dose FBP recon (b) due to high noise content. This display window is [-160, 240]HU.

(Figs. 6g and 8g) than the other networks, while the CNN-VGG and WGAN-VGG images are visually more similar to the NDCT images. This is because the VGG loss used in CNN-VGG and WGAN-VGG is computed in a feature space that is trained previously on a very large natural image dataset [46]. By using VGG loss, we transferred the knowledge of human perception that is embedded in VGG network to CT image quality evaluation. The performance of using WGAN alone is not acceptable because it only maps the data distribution from LDCT to NDCT but does not guarantee the image content correspondence. As for the lesion detection in these two slices, all the networks enhance the lesion visibility compared to the original noisy low dose FBP images as noise is reduced by

the different approaches.

As for iterative reconstruction technique, the implemented dictionary learning reconstruction (DictRecon) result gave the most aggressive noise reduction effect compared to the network outputs. However, it over-smoothed some fine structures. For example, in Fig. 8, the vessel pointed by the green arrow was smeared out while it is easily identifiable in NDCT as well as WGAN-VGG images.

E. Quantitative Analysis

For quantitative analysis, we calculated the peak-to-noise ratio (PSNR) and structural similarity (SSIM). The summary data are in Table I. CNN-MSE ranks the first in terms of

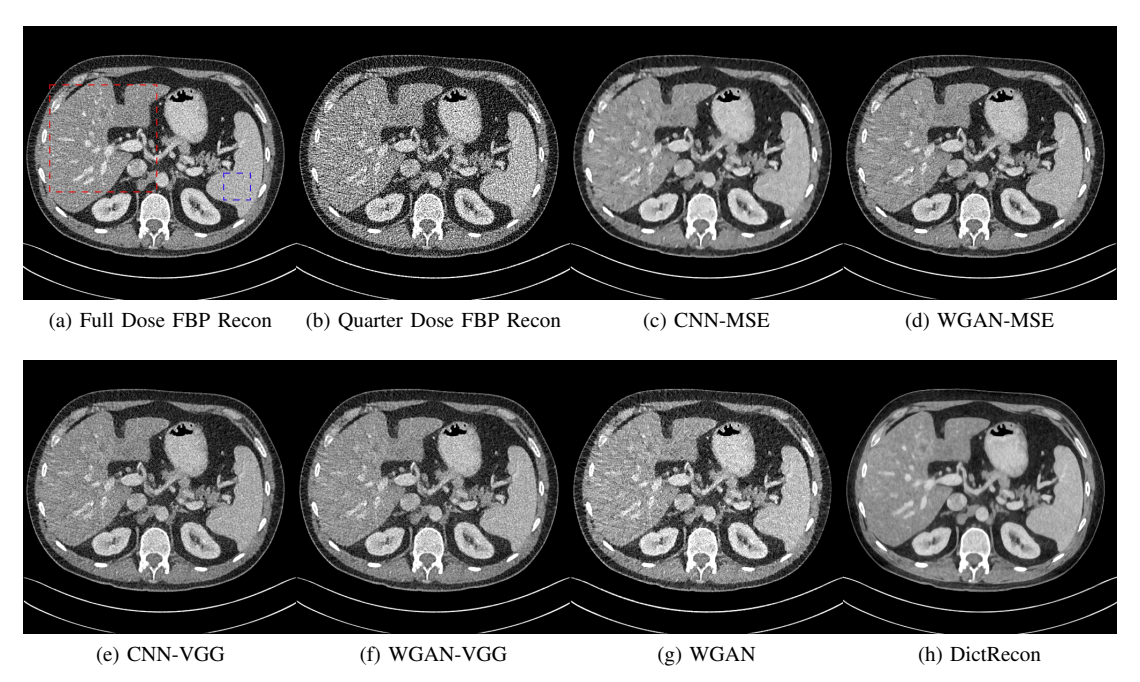


Fig. 7. Transverse CT images of the abdomen demonstrate small low attenuation liver lesions. The display window is [-160, 240]HU.

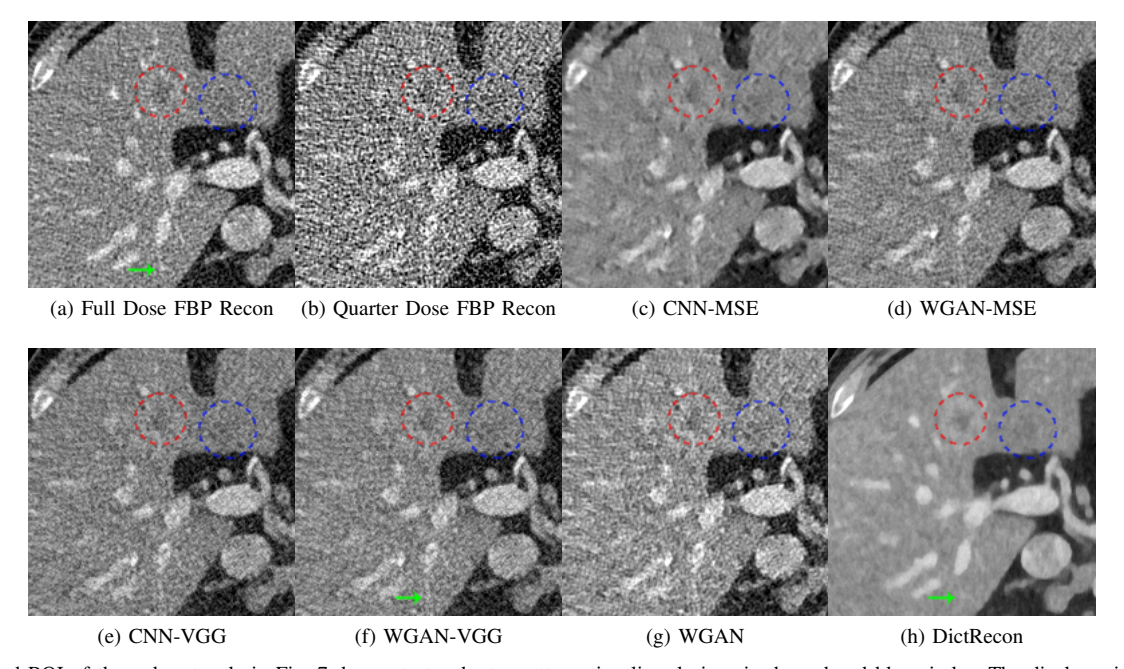


Fig. 8. Zoomed ROI of the red rectangle in Fig. 7 demonstrates the two attenuation liver lesions in the red and blue circles. The display window is [-160, 240]HU.

PSNR, while WGAN is the worst. Since PSNR is equivalent to the per-pixel loss, it is not surprising that CNN-MSE, which was trained to minimize MSE loss, outperformed the networks trained to minimize other feature-based loss. It is worth noting that these quantitative results are in decent agreement with Fig. 4, in which CNN-MSE has the smallest MSE loss and WGAN has the largest. The reason why WGAN ranks the worst in PSNR and SSIM is because it does not include either MSE or VGG regularization. DictRecon did achieves the best SSIM and a high PSNR. However, it has the problem

of image blurring and leads to blocky and waxy artifacts in the resultant images. This indicates that PSNR and SSIM may not be sufficient in evaluating image quality.

Furthermore, in order to gain more insight into the output images from different approaches, we inspect the statistical properties by calculating the mean CT numbers (Hounsfield Units) and standard deviations (SDs) of two flat regions in Figs. 5 and 7 (marked by the blue rectangles). In an idea scenario, a noise reduction algorithm should achieve mean and SD to NDCT images as close as possible. As shown

in Table II, Both CNN-MSE and DictRecon produced much smaller SDs compared to NDCT, which indicates they over-smoothed the images and supports our visual observation. On the contrary, WGAN produced the closest SDs yet smaller mean values, which means it can reduce noise to the same level as NDCT but it compromised the information content. On the other hand, the proposed WGAN-VGG has outperformed CNN-VGG, WGAN-MSE and other selected methods in terms of mean CT numbers, SDs, and most importantly visual impression.

IV. DISCUSSIONS AND CONCLUSION

The single most important motivation for this paper is to approach the gold standard NDCT images as much as possible. As described above, the feasibility and merits of GAN has been investigated for this purpose with the Wasserstein distance and the VGG loss. The difference between using the MSE and VGG losses are rather significant. Despite the fact that networks with MSE would offer higher values for traditional figures of merit, VGG loss based networks seem desirable for better visual image quality with more details and less artifacts.

The experimental results have demonstrated that using WGAN helps improve image quality and statistical properties. Comparing the images of CNN-MSE and WGAN-MSE, we can see that the WGAN framework helped avoid oversmoothing effect typically suffered by MSE based image generators. Although CNN-VGG and WGAN-VGG visually share a similar result, the quantitative analysis shows WGAN-VGG enjoys higher PSNRs and more faithful statistical properties of denoised images relative to those of NDCT images. However, using WGAN alone WGAN alone reduced noise but at the expense of losing critical features. The resultant images do not show a strong noise reduction. Quantitatively, the associated PSNR and SSIM increased modestly compared to LDCT but they are much lower than what the other networks produced.

The denoising network is a typical end-to-end operation, in which the input is a LDCT image while the target is a NDCT image. Although we have generated images visually similar to NDCT counterparts in the WGAN-VGG network, we recognize that these generated images are still not as good as NDCT images. Moreover, noise still exists in NDCT images. Thus, it is possible that VGG network has captured these noise features and kept them in the denoised images. This could be a common problem for all the denoising networks. How to outperform the so-called gold standard NDCT images is an interesting open question.

In conclusion, we have proposed a contemporary deep neural network that uses a WGAN framework with perceptual loss function for LDCT image denoising. Instead of focusing on the design of a complex network structure, we have dedicated our effort to combine synergistic loss functions that guide the denoising process so that the resultant denoised results are as close to the gold standard as possible. Our experiment results with real clinical images have shown that the proposed WGAN-VGG network can effectively solve the well-known over-smoothing problem and generate images with

reduced noise and increased contrast for improved lesion detection. In the future, we plan to incorporate the WGAN-VGG network with more complicated generators such as the networks reported in [27], [41] and extend these networks for image reconstruction from raw data by making a neural network counterpart of the FBP process.

REFERENCES

- [1] D. J. Brenner and E. J. Hall, "Computed tomography an increasing source of radiation exposure," *New England Journal of Medicine*, vol. 357, no. 22, pp. 2277–2284, 2007.
- [2] A. B. De Gonzalez and S. Darby, "Risk of cancer from diagnostic x-rays: estimates for the uk and 14 other countries," *The lancet*, vol. 363, no. 9406, pp. 345–351, 2004.
- [3] J. Wang, H. Lu, T. Li, and Z. Liang, "Sinogram noise reduction for low-dose ct by statistics-based nonlinear filters," in *Proc. of SPIE Vol*, vol. 5747, 2005, p. 2059.
- [4] J. Wang, T. Li, H. Lu, and Z. Liang, "Penalized weighted least-squares approach to sinogram noise reduction and image reconstruction for low-dose x-ray computed tomography," *IEEE transactions on medical* imaging, vol. 25, no. 10, pp. 1272–1283, 2006.
- [5] A. Manduca, L. Yu, J. D. Trzasko, N. Khaylova, J. M. Kofler, C. M. McCollough, and J. G. Fletcher, "Projection space denoising with bilateral filtering and ct noise modeling for dose reduction in ct," *Medical physics*, vol. 36, no. 11, pp. 4911–4919, 2009.
- [6] M. Beister, D. Kolditz, and W. A. Kalender, "Iterative reconstruction methods in x-ray ct," *Physica medica*, vol. 28, no. 2, pp. 94–108, 2012.
- [7] A. K. Hara, R. G. Paden, A. C. Silva, J. L. Kujak, H. J. Lawder, and W. Pavlicek, "Iterative reconstruction technique for reducing body radiation dose at ct: feasibility study," *American Journal of Roentgenology*, vol. 193, no. 3, pp. 764–771, 2009.
- [8] J. Ma, J. Huang, Q. Feng, H. Zhang, H. Lu, Z. Liang, and W. Chen, "Low-dose computed tomography image restoration using previous normal-dose scan," *Medical physics*, vol. 38, no. 10, pp. 5713–5731, 2011.
- [9] Y. Chen, X. Yin, L. Shi, H. Shu, L. Luo, J.-L. Coatrieux, and C. Toumoulin, "Improving abdomen tumor low-dose CT images using a fast dictionary learning based processing," *Physics in medicine and biology*, vol. 58, no. 16, p. 5803, 2013.
- [10] P. F. Feruglio, C. Vinegoni, J. Gros, A. Sbarbati, and R. Weissleder, "Block matching 3d random noise filtering for absorption optical projection tomography," *Physics in medicine and biology*, vol. 55, no. 18, p. 5401, 2010.
- [11] B. De Man and S. Basu, "Distance-driven projection and backprojection in three dimensions," *Physics in medicine and biology*, vol. 49, no. 11, p. 2463, 2004.
- [12] R. M. Lewitt, "Multidimensional digital image representations using generalized kaiser-bessel window functions," *JOSA A*, vol. 7, no. 10, pp. 1834–1846, 1990.
- [13] B. R. Whiting, P. Massoumzadeh, O. A. Earl, J. A. O'Sullivan, D. L. Snyder, and J. F. Williamson, "Properties of preprocessed sinogram data in x-ray computed tomography," *Medical physics*, vol. 33, no. 9, pp. 3290–3303, 2006.
- [14] I. A. Elbakri and J. A. Fessler, "Statistical image reconstruction for polyenergetic x-ray computed tomography," *IEEE transactions on medical imaging*, vol. 21, no. 2, pp. 89–99, 2002.
- [15] S. Ramani and J. A. Fessler, "A splitting-based iterative algorithm for accelerated statistical x-ray ct reconstruction," *IEEE transactions on medical imaging*, vol. 31, no. 3, pp. 677–688, 2012.
- [16] E. Y. Sidky and X. Pan, "Image reconstruction in circular cone-beam computed tomography by constrained, total-variation minimization," *Physics in medicine and biology*, vol. 53, no. 17, p. 4777, 2008.
- [17] Y. Liu, J. Ma, Y. Fan, and Z. Liang, "Adaptive-weighted total variation minimization for sparse data toward low-dose x-ray computed tomography image reconstruction," *Physics in medicine and biology*, vol. 57, no. 23, p. 7923, 2012.
- [18] Z. Tian, X. Jia, K. Yuan, T. Pan, and S. B. Jiang, "Low-dose ct reconstruction via edge-preserving total variation regularization," *Physics in medicine and biology*, vol. 56, no. 18, p. 5949, 2011.
- [19] Q. Xu, H. Yu, X. Mou, L. Zhang, J. Hsieh, and G. Wang, "Low-dose x-ray ct reconstruction via dictionary learning," *IEEE Transactions on Medical Imaging*, vol. 31, no. 9, pp. 1682–1697, 2012.

- [20] Y. Zhang, X. Mou, G. Wang, and H. Yu, "Tensor-based dictionary learning for spectral ct reconstruction," *IEEE transactions on medical imaging*, vol. 36, no. 1, pp. 142–154, 2017.
- [21] G. Wang, M. Kalra, and C. G. Orton, "Machine learning will transform radiology significantly within the next 5 years," *Medical Physics*, 2017.
- [22] G. Wang, "A perspective on deep imaging," *IEEE Access*, vol. 4, pp. 8914–8924, 2016.
- [23] C. Dong, C. C. Loy, K. He, and X. Tang, "Image super-resolution using deep convolutional networks," *IEEE Trans. Pattern Anal. Mach. Intell.*, vol. 38, no. 2, pp. 295–307, 2016.
- [24] H. Chen, Y. Zhang, W. Zhang, P. Liao, K. Li, J. Zhou, and G. Wang, "Low-dose CT denoising with convolutional neural network," 2016. [Online]. Available: arXiv:1610.00321
- [25] O. Ronneberger, P. Fischer, and T. Brox, "U-net: Convolutional networks for biomedical image segmentation," in *International Conference* on Medical Image Computing and Computer-Assisted Intervention. Springer, 2015, pp. 234–241.
- [26] H. Chen, Y. Zhang, M. K. Kalra, F. Lin, Y. Chen, P. Liao, J. Zhou, and G. Wang, "Low-dose ct with a residual encoder-decoder convolutional neural network (red-cnn)," *IEEE Transactions on Medical Imaging*, p. 11, 2017.
- [27] E. Kang, J. Min, and J. C. Ye, "A deep convolutional neural network using directional wavelets for low-dose x-ray ct reconstruction," arXiv preprint arXiv:1610.09736, 2016.
- [28] J. Johnson, A. Alahi, and L. Fei-Fei, "Perceptual losses for realtime style transfer and super-resolution," 2016. [Online]. Available: arXiv:1603.08155
- [29] C. Ledig, L. Theis, F. Huszar, J. Caballero, A. Cunningham, A. Acosta, A. Aitken, A. Tejani, J. Totz, Z. Wang, and W. Shi, "Photo-realistic single image super-resolution using a generative adversarial network," 2016. [Online]. Available: arXiv:1609.04802
- [30] M. Arjovsky, S. Chintala, and L. Bottou, "Wasserstein gan," arXiv preprint arXiv:1701.07875, 2017.
- [31] I. Goodfellow, J. Pouget-Abadie, M. Mirza, B. Xu, D. Warde-Farley, S. Ozair, A. Courville, and Y. Bengio, "Generative adversarial nets," in Advances in neural information processing systems, 2014, pp. 2672– 2680
- [32] I. Goodfellow, "Nips 2016 tutorial: Generative adversarial networks," arXiv preprint arXiv:1701.00160, 2016.
- [33] A. Brock, T. Lim, J. M. Ritchie, and N. Weston, "Neural photo editing with introspective adversarial networks," arXiv preprint arXiv:1609.07093, 2016.
- [34] J.-Y. Zhu, P. Krähenbühl, E. Shechtman, and A. A. Efros, "Generative visual manipulation on the natural image manifold," in *European Con*ference on Computer Vision. Springer, 2016, pp. 597–613.
- [35] P. Isola, J.-Y. Zhu, T. Zhou, and A. A. Efros, "Image-to-image translation with conditional adversarial networks," arXiv preprint arXiv:1611.07004, 2016.
- [36] D. Nie, R. Trullo, C. Petitjean, S. Ruan, and D. Shen, "Medical image synthesis with context-aware generative adversarial networks," arXiv preprint arXiv:1612.05362, 2016.
- [37] M. Arjovsky and L. Bottou, "Towards principled methods for training generative adversarial networks," in NIPS 2016 Workshop on Adversarial Training. In review for ICLR, vol. 2016, 2017.
- [38] I. Gulrajani, F. Ahmed, M. Arjovsky, V. Dumoulin, and A. Courville, "Improved training of wasserstein gans," arXiv preprint arXiv:1704.00028, 2017.
- [39] M. Nixon and A. S. Aguado, Feature Extraction & Image Processing, 2nd ed. Academic Press, 2008.
- [40] K. Simonyan and A. Zisserman, "Very deep convolutional networks for large-scale image recognition," 2014. [Online]. Available: arXiv: 1409.1556
- [41] H. Chen, Y. Zhang, M. K. Kalra, F. Lin, P. Liao, J. Zhou, and G. Wang, "Low-dose ct with a residual encoder-decoder convolutional neural network (red-cnn)," arXiv preprint arXiv:1702.00288, 2017.
- [42] S. Srinivas, R. K. Sarvadevabhatla, K. R. Mopuri, N. Prabhu, S. S. S. Kruthiventi, and R. V. Babu, "A taxonomy of deep convolutional neural nets for computer vision," *CoRR*, 2016. [Online]. Available: arXiv:1601.06615
- [43] AAPM, "Low dose ct grand challenge," 2017. [Online]. Available: http://www.aapm.org/GrandChallenge/LowDoseCT/#
- [44] D. Kingma and J. Ba, "Adam: A method for stochastic optimization," arXiv preprint arXiv:1412.6980, 2014.
- [45] M. Abadi, A. Agarwal, P. Barham, E. Brevdo, Z. Chen, C. Citro, G. S. Corrado, A. Davis, J. Dean, M. Devin *et al.*, "Tensorflow: Large-scale machine learning on heterogeneous distributed systems," *arXiv preprint arXiv:1603.04467*, 2016.

[46] J. Deng, W. Dong, R. Socher, L.-J. Li, K. Li, and L. Fei-Fei, "ImageNet: A Large-Scale Hierarchical Image Database," in *CVPR09*, 2009.